JCTC Journal of Chemical Theory and Computation

Computation of Local and Global Properties of the Electron Localization Function Topology in Crystals

J. Contreras-García, A. Martín Pendás, and J. M. Recio*

MALTA-Consolider Team and Departamento de Química Física y Analítica, Universidad de Oviedo, E-33006 Oviedo, Spain

B. Silvi

Laboratoire de Chimie Théorique (UMR-CNRS 7616), Université Pierre et Marie Curie, 3 rue Galilée 94200-Ivry sur Seine, France

Received October 6, 2008

Abstract: We present a novel computational procedure, general, automated, and robust, for the analysis of local and global properties of the electron localization function (ELF) in crystalline solids. Our algorithm successfully faces the two main shortcomings of the ELF analysis in crystals: (i) the automated identification and characterization of the ELF induced topology in periodic systems, which is impeded by the great number and concentration of critical points in crystalline cells, and (ii) the localization of the zero flux surfaces and subsequent integration of basins, whose difficulty is due to the diverse (in many occasions very flat or very steep) ELF profiles connecting the set of critical points. Application of the new code to representative crystals exhibiting different bonding patterns is carried out in order to show the performance of the algorithm and the conceptual possibilities offered by the complete characterization of the ELF topology in solids.

I. Introduction

Due to the high coordination indexes and to the numerous atom−atom contacts, the presence of different bonding types is a common and genuine feature of solids which hampers their characterization when compared with the molecular realm. Performing a rigorous qualitative and quantitative classification of these bonds, based on a unique theoretical formalism, has revealed itself to be a challenge and a source of debate.[1] The localization of orbitals leads to ambiguities in many solid-state problems,[2] a reason for which the topological analysis in real space has been shown to be a very fruitful approach in the last few decades. Among these methods, the widest-spread approach has been to consider the topological analysis of the electron density (AIM) as developed by Bader and co-workers,[3,4] according to which the existence of a bond is associated to the presence of a bond path in the stable structure of the solid. It has also been long recognized that chemical insight into the nature of the chemical bond can be gained by resorting to the electron localization function (ELF).[5]

The topological analysis of ELF, although spread among molecules, has been scarce in the solid state due to the major computational difficulties imposed by periodicity.[5−7] Some noticeable applications concern relevant geophysical problems, as the identification of favored docking sites in SiO_2 polymorphs,[8,9] whereby protons were found to prefer the proximities of lone pairs. However, the ability of this function to reflect interactions, as well as the translational symmetry of crystalline systems, leads to an intricate pattern of ELF critical points and of irregular ELF profiles that hamper their automated localization and the integration of the related basins in which the 3D space of the unit cell is divided.

Our work has been focused on the development of a computational algorithm attempting to fulfill the gap existing between the ELF topological analyses of bonding in the molecular and the crystalline realms. A thoughtful analysis of the nature of the problem is critical thereto. It was already recognized by Nathaniel et al.[10] that algorithms coming from

* Corresponding author. E-mail: mateo@fluor.quimica.uniovi.es.

10.1021/ct800420n CCC: $40.75
Published on Web 12/15/2008

Bader analyses mainly fail at the inner and outer core, whose sphericity remains practically unaltered under the crystal environment, leading to nearly degenerated surfaces and critical point clustering. A hybrid algorithm that combines previous methods and a new approach for the determination of the local and global properties of the core topology is proposed for the complete determination of the ELF topology. Due to the intricate and heterogeneous nature of the function, special emphasis has been given to the design of a robust algorithm, of applicability to a wide variety of crystal bonding patterns.

The organization of the paper is as follows. First, we will introduce the basic concepts of the ELF topology stressing the computational difficulties associated with the main differences between the ELF in the molecular and the crystalline realms. Then, we explain the algorithms devised to overcome these problems for the localization of critical points and the integration of basins. Next, some examples of bonding analyses in prototypical solids will be presented to show the robustness and performance of the method. Finally, conclusions will be drawn and future applications advanced.

II. ELF Topological Analysis in Crystals

The electron localization function (ELF) was originally designed by Becke and Edgecombe to identify "localized electronic groups in atomic and molecular systems".[11] It relies, through its kernel, to the laplacian of the conditional same spin pair probability scaled by the homogeneous electron gas kinetic energy:

$$\chi_\sigma(\mathbf{r}) = \frac{D_\sigma(\mathbf{r})}{D_\sigma^0(\mathbf{r})} \tag{1}$$

in which

$$D_\sigma(\mathbf{r}) = \tau_\sigma(\mathbf{r}) - \frac{1}{4}\frac{(\rho_\sigma(\mathbf{r}))^2}{\rho_\sigma(\mathbf{r})}$$

appears to be the difference of the actual definite positive kinetic energy $\tau_\sigma(\mathbf{r})$ and the von Weizsäcker kinetic energy functional,[12] whereas

$$D_\sigma^0(\mathbf{r}) = \frac{3}{5}(6\pi^2)^{2/3}\rho_\sigma^{5/3}(\mathbf{r})$$

is the kinetic energy density of the homogeneous electron gas. This formulation led Savin to propose an interpretation of ELF in terms of the local excess kinetic energy due to the Pauli repulsion, enabling its calculation from Kohn−Sham orbitals.[2,13,14] Orbital based interpretations of ELF have been proposed by Burdett[15] and more recently by Nalewajski et al.[16] who considered the nonadditive interorbital Fisher information. Another route pioneered by Dobson[17] explicitly considers the pair functions. It has been independently developed by Kohout et al.[18,19] and by one of us[20] allowing the extension of ELF to correlated wave functions.[21]

From a simple statistical viewpoint, the concept of electron density localization at a given position $\mathbf{r}$ relies on the standard deviation of the electron density integrated over a sampling volume $V(\mathbf{r})$ encompassing the reference point and containing a given quantity of matter, in other words a given charge q. The smaller the standard deviation, the higher the localization. Instead of the standard deviation, it is advantageous to use its square, the variance σ^2, which can be expressed as the expectation value of the variance operator:[22]

$$\langle \widehat{\mathrm{cov}}(V(\mathbf{r}), V(\mathbf{r}))\rangle = \bar{\Pi}(V(\mathbf{r}), V(\mathbf{r})) - \bar{N}(V(\mathbf{r}))\left(\bar{N}(V(\mathbf{r})) - 1\right) = \bar{\Pi}(V(\mathbf{r}), V(\mathbf{r})) - q^2 + q \tag{2}$$

in which $\bar{N}(V(\mathbf{r})) = q$ and $\bar{\Pi}(V(\mathbf{r}), V(\mathbf{r}))$ are respectively the one particle and two particle densities integrated over the sample $V(\mathbf{r})$. In the expression of the variance given above, only $\bar{\Pi}(V(\mathbf{r}), V(\mathbf{r}))$ is function of the position and therefore $-q^2 + q$ can be regarded as a constant and deleted. The integrated pair density is the sum of an opposite spin contribution, $2\bar{\Pi}^{\alpha\beta}(V(\mathbf{r}),V(\mathbf{r}))$ almost proportional to q^2 and of a same spin contribution $\bar{\Pi}^{\alpha\alpha}(V(\mathbf{r}), V(\mathbf{r})) + \bar{\Pi}^{\beta\beta}(V(\mathbf{r}), V(\mathbf{r}))$ which has numerically been shown proportional to a function of the position, say $c_\pi(\mathbf{r})$, times $q^{5/3}$. In the limit $q = 0$, the ratio

$$\frac{\bar{\Pi}(V(\mathbf{r}), V(\mathbf{r}))}{q^{5/3}}$$

tends to the spin pair composition, $c_\pi(\mathbf{r})$, a local function independent of the size of the sample.[20] The ability of this function to localize "electronic groups" can be illustrated by a very simple example in which two α and two β spin electrons are confined in a box of volume Ω. For the sake of simplicity we assume the electron density probability to be uniform, i.e. $\rho(\mathbf{r}) = 4/\Omega$ without spin polarization ($\rho^\alpha(\mathbf{r}) = \rho^\beta(\mathbf{r}) = 2/\Omega$), such as the opposite spin pair functions, $\Pi^{\alpha\beta}(\mathbf{r}_1, \mathbf{r}_2) = \Pi^{\beta\alpha}(\mathbf{r}_1, \mathbf{r}_2) = 4/\Omega^2$ are constant. This model enables to consider two localization cases. On the one hand, the opposite spin pairs are delocalized over the box and the same spin pair functions are constant: $\Pi^{\alpha\alpha}(\mathbf{r}_1, \mathbf{r}_2) = \Pi^{\beta\beta}(\mathbf{r}_1, \mathbf{r}_2) = 2/\Omega^2$ and therefore $c_\pi(\mathbf{r})$ is also constant. On the other hand, each opposite spin pair occupies one-half of the box such as the following:

$$\Pi^{\alpha\alpha}(\mathbf{r}_1, \mathbf{r}_2) = \Pi^{\beta\beta}(\mathbf{r}_1, \mathbf{r}_2) = \begin{cases} 0 & \mathbf{r}_1, \mathbf{r}_2 \in \text{ same half box} \\ 4/\Omega^2 & \mathbf{r}_1, \mathbf{r}_2 \in \text{ different half boxes} \end{cases} \tag{3}$$

It follows that

$$c_\pi(\mathbf{r}) \begin{cases} = 0 & \mathbf{r} \notin \text{ the boundary} \\ \propto 4/\Omega^2 & \mathbf{r} \in \text{ the boundary} \end{cases} \tag{4}$$

which enables one to locate the boundary between the two opposite spin pair regions.

For the Hartree−Fock wave function, it can be easily demonstrated[20] that

$$\chi_\sigma(\mathbf{r}) \approx c_\pi(\mathbf{r}) \tag{5}$$

The localization function itself is obtained through the transformation of $\chi_\sigma(\mathbf{r})$ into a Lorentzian function

$$\eta(\mathbf{r}) = \frac{1}{1 + \chi_\sigma^{\,2}(\mathbf{r})} \tag{6}$$

so that it tends to 1 in those regions where the localization is high and to small values at the boundaries between such regions.

The arguments developed above indicate that $\eta(\mathbf{r})$ can be used to recover regions of space associated to electron pairs as they emerge in the Lewis's description.[23] The dynamical system theory[24] has been used in this context to provide a partition of the direct geometrical space into non overlapping basins of attractors[25,26] which can be thought of as electronic domains corresponding to the chemical entities of the Lewis's picture. Moreover, it has been recently shown that the electrostatic repulsions between these basins provide a justification of the valence shell electron pair repulsion (VSEPR) rules.[27] The ELF basins belong either to the core or valence shells of atoms in molecules. The valence basins V(A, ...) encompassing a given atomic core basin C(A) (which can be constituted by K, L, ... shells) form the valence shell of atom A. In agreement with the Lewis's picture V(A, ...) may belong to several atomic shells. The synaptic order of a valence basin is the number of atomic shells to which it belongs. The hierarchy of the ELF basin is given by the bifurcation diagrams[28,29] which provide the connectivity of the different fragments of the investigated system.

Within the dynamical system framework, pioneered by Bader for the analysis of the electron density,[3] a formal analogy is made between a vector field bounded on a manifold and a velocity field. In the present case, the vector field is the gradient field of the ELF, $\nabla\eta(\mathbf{r})$, and the manifold the 3-dimensional geometrical space. This is the reason why this point is also known as attractor of the gradient field. Attractors belong to a subset of special points of the field, named critical points (CPs), characterized by a null gradient. Contrary to wandering points ($\nabla\eta \neq 0$) critical points may act as a source or a sink of more than one gradient path, depending on their nature. The number of nonzero eigenvalues of the Hessian, or rank, determines its dimensionality, and the sum of the signs of the Hessian eigenvalues characterizes the capability to receive or send gradient paths. In a stable 3D topology, this gives rise to the following possibilities: (3, −3) for local maxima or attractors, (3, +3) for local minima, and (3, −1) and (3, +1) for saddle points in one or two dimensions, respectively.

Indeed, two types of topological information are obtained: local and global. Local information is gathered by evaluating density properties at distinctive points where the gradient vanishes. Global information is acquired from volume integration of property densities over spatial fragments. Since the topological analysis of the ELF gradient field[25,26] yields basins that can be associated to Lewis entities, the integration of the density (ρ) over their volume (Ω_i) assigns a population ($\bar{N}$) to bonds, lone pairs and atomic shells:

$$\bar{N}(\Omega_i) = \int_{\Omega_i} \rho(\mathbf{r})\mathrm{d}\mathbf{r} \tag{7}$$

In spite of the lack of a clear physical significance of the definition of the zero flux surfaces of ELF, it was demonstrated by Kohout and Savin[30] that these populations follow the expected values and tendencies from the Aufbau principle and the VSEPR theory.

The properties of the gradient dynamical system are complemented in the context of the ELF topology with the interpretation derived from the *f*-domain[28] concept, that enables chemical units in the system to be recovered, as well as to characterize the basins according to common chemical knowledge. Introduced by Mezey[31] within the AIM framework, the concept of an *f*-domain accounts for the volume enclosed by an isosurface of a certain value of $\eta = f$. As the value f increases, successive splitting of the initial domains take place until all of them contain one, and only one, attractor. This process in called reduction (and the final domains, irreducible), and the order in which it takes place reveals the nature of the interactions taking place in the system and the relationship between basins. The turning points of the splitting corresponds to that of the highest (3, −1) point of the separatrix connecting the basins. According to the value of η at these nodes, also known as *bips* (bond interaction points),[32] a bifurcation tree can be constructed that reveals the basin hierarchy at a glance. The difficulties that the localization of all the bips entail in solids have refrained the use of bifurcation diagrams for their bond analysis in spite of the wide range of possibilities this would obviously offer[5] due to the intricate and colorful bonding patterns present in the solid state.

There are several factors that draw a clear line between the molecular and the crystalline realms as far as the study of their topology is concerned. On the one hand, and due to the periodicity of the solid, an infinite number of critical points is expected. The search has to be, therefore, limited to a finite part of the solid (generally the unit cell or one part of it). This fact obliges the implementation of periodic contour conditions that ensure the recuperation of the points escaping this region of space. Furthermore, for the electron localization function defined over the crystalline unit cell, the Morse relationship that holds reads as follows:

$$n_{(3,-3)} - n_{(3,-1)} + n_{(3,+1)} - n_{(3,+3)} = 0 \tag{8}$$

$$n_{(3,-3)} \geq 1, \quad n_{(3,-1)} \geq 3, \quad n_{(3,+1)} \geq 3, \quad n_{(3,+3)} \geq 1 \tag{9}$$

being n the number of critical points of a given type. Just like in the topology of molecules, the (3, −3) positions are associated to Lewis entities of the crystal. The existence of (3, +3) points is ensured by the Weierstrass theorem, which accordingly enforces the presence of the whole set of types of critical points of rank 3 (eq 9).

The split of the critical points imposed by symmetry had already been observed when passing from the atomic to the molecular state. The neighboring atoms force the degenerated atomic ELF maxima to collapse onto nondegenerated ones.[25] Due to the high coordinations in solid state, great concentration of critical points cluster in small volumes. This great variety and amount of critical points per unit cell sets the main algorithmic difference between solids and molecules.[4] Thus, algorithms as the one used in AIMPAC[33] where critical points are searched by an exhaustive formation of pairs, trios, and quartets of atoms are not suitable due to the translational periodicity of the system, and new algorithms have to be designed that benefit from the properties induced by the translational symmetry. For example, the periodicity of the solid ensures the cancellation of the gradient at the fixed

Wyckoff positions, providing some a priori information on the CPs of the system. As far as integrations are concerned, the periodicity in the solid assures finite values for all the basins in the crystal, so that no thresholds are needed to delimit volumes because all basin properties are well defined.

III. Algorithm

A. Construction of the Critical Point List. The clustering of critical points that takes place in the ELF topology of crystals gives rise to two undesirable computational features: (i) finding a great number of solutions of a non linear system of equations within a small interval of the domain of the variables and (ii) being able to accurately discard equivalent solutions. Since the valence region has been found to be exhaustively tracked by algorithms analogous to those employed for the analysis of the topology induced by the electron density, the complete characterization of the ELF topology in the solid requires a hybrid method, with a combination of core−valence approaches. In the first place, we have resorted to a recursive and exhaustive method implemented in our laboratory[34] for the construction of the critical point list of the electron density field of crystals. It starts with the division of the unit cell (or its irreducible part) into all the irreducible tetrahedra it is formed of. Then, all the 0−3-dimensional simplexes are generated in order to perform an iterative barycentric search in each of them: a critical point is searched inside the N simplex that gives rise to a new subdivision into $N + 1$ simplexes that share this barycenter as a common vertex. An infinite recurrence is avoided by introducing a limiting number of subdivisions. This method would ideally be able to localize all the critical points of the crystal, as long as the algorithm is able to find one critical point, if present, inside a simplex. This is the case of the valence region but not of the cores. As the simplexes evolve toward the core regions, the concentration of steep gradients is such that the recursive procedure fails in exhausting the solutions.

However, the landscape of the ELF topology in the cores is extremely simple and constant from one crystal to another, enabling to devise a complementary search that completes the set of critical points found in the first step.[10] Cores are characterized by a nearly spherical shape of the shells enclosed within it. Provided that this structure remains nearly unperturbed in the crystalline environment, we can perform a second CP search around the nuclei, seeding the shell radii as starting points. In order to devise a completely automated search, these positions are internally approximated around a spherical grid by the $\partial\eta(\theta, \phi)/\partial r = 0$ points. The resulting hybrid method turns out to be highly efficient and able to automatically provide complete sets of critical points. Ill cases are mainly related to heavy elements inner cores, whose shells are very abrupt. Although these points do not provide chemical insights, a wise set of parameters provided by the user in order to accurately determine the shell radii and discard equivalent positions would provide the fussy user with the answer.

If the first search is carried out in the irreducible Wigner Seitz cell, some of the borders of the tetrahedra may coincide, leading to redundant critical points. Repeated critical points would also be found according to their multiplicity in the restricted second search and in the barycentric one, were it carried out in the unit cell. Thus, all temporal positions are subsequently filtered for repetitions with the help of punctual symmetry operations and applying cutoffs to avoid redundancies due to numerical inaccuracies. To the best of our knowledge, this algorithm has been the first to provide complete lists of critical points of the ELF induced topology. Not only does it output the position of the maxima for the ulterior integration of their basins, but it also informs about the delocalization between them.

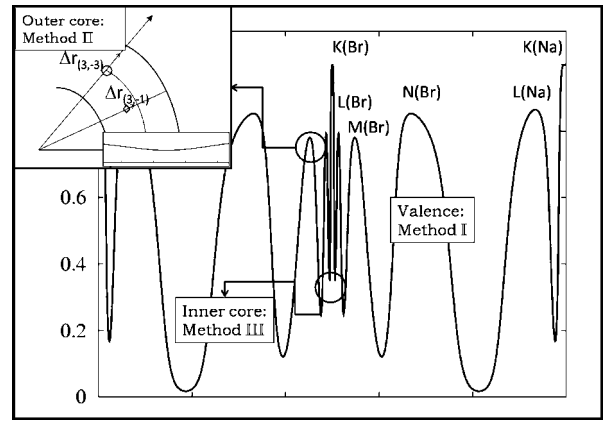

Figure 1. Zone of application of each of the methods described in the text in the NaBr crystal. Method I is able to resolve the valence topology (4th N-shell of Br^- and L-shell of Na^+) flat profiles in the shell basins in the θ, ϕ direction represented in the inset are avoided by means of method II, that enables a more accurate and fast integration of the Br^- outercore. The localization of the quasi-degenerated zero flux surfaces in the inner core of Br^- K-shell is avoided by the spherical approximation of method III.

The concepts of localization domain and bifurcation tree have been rarely used in the solid state, in spite of their potentiality, due to the difficult determination of the bip points by graphical approaches. In fact, its use was already encouraged by Gatti in order to shed light into the nature of the interactions governing the structure of molecular solids.[5] The complete characterization of the topology of the ELF gradient offered by our core−valence algorithm holds the key for a direct construction of bifurcation trees[35] within the crystalline realm, as proved in our recent studies on the pressure behavior of BeO phases[36] and the CO_2 polymerization.[37]

B. Basin Integration. The integration of the basins of the electron density has been the object of numerous publications due to the difficulty of reaching a balance between computational time and accuracy. The first attempts, led by Biegler-König et al.,[33,38] were based on the spatial localization of the zero flux surfaces. Less time-consuming proposals were subsequently put forward by the group of Popelier et al., who devised numerous ingenious ways to tackle the problem, from the analytical fitting of the surfaces[39,40] to the discretization of basins into polyhedra.[41] Grids have also been a very popular modality[33,38] due to their speed. Indeed, the integration of more complex topologies has been mainly addressed by means of the later

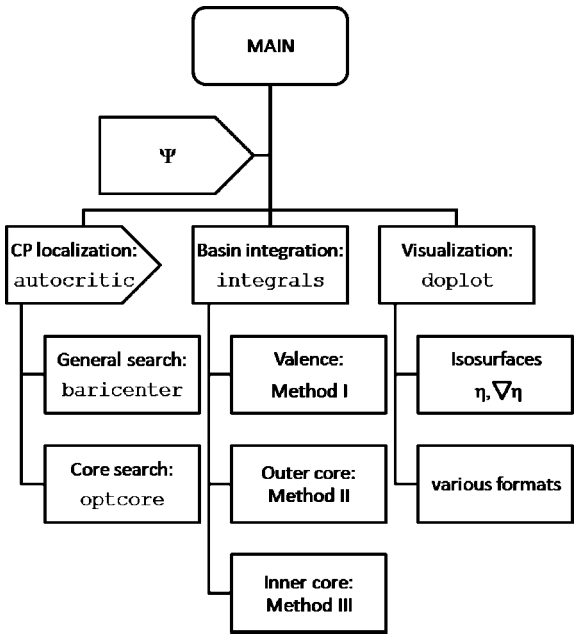

Figure 2. Schematic figure of the code operation.

approach[42,43] to the detriment of accuracy.[44] Since sharp as well as nearly degenerated basins are a common feature of the ELF induced topology, we have decided to recover the more accurate ELF basins properties, as well as an explicit picture of their shape provided by the first set of methods, which are known to deal properly with complicated basin shapes and heterogeneous function profiles, and then using chemical knowledge to properly solve the problem.

Valence basins occupy broad spaces and their profiles are smooth enough to be accurately tracked by the type of methods mentioned above. Its ability to integrate valence basins is highlighted in Figure 1 as the proper method to obtain basin properties of the 4th N-shell of Br^- in NaBr under the name of method I. Due to the colorful valence shapes depending on the bonding type, the bisection method[40] has been preferred due to its accuracy, and in spite of its computational cost. First, and making use of the previous algorithm for the determination of the (3, −3) points, a mapping is carried out for each attractor, centering at its location a polar coordinate system. Then, this sphere is divided into a regular $n_\theta \times n_\phi$ grid, whose radial lengths are found according to the flux lines properties. Since all the gradient paths that end up at the given attractor belong to its basin, it suffices to bracket the point $r(\theta, \phi)$ at which the flux lines start leading to another (3, −3) point. Given the fact that we have reduced the problem to one dimension, a bisection search is, due to its reliability, mostly suited for this task. It should be noted that the wide range of valence basin shapes difficulties an automated setting of the bisection initial limits and would boost Newton−Raphson weaknesses at long distances, so the point fulfilling the condition $\partial\eta/\partial r = 0$ can be used as the first approximation for setting the limits. Finally, and once the radial limit has been found, the Gaussian−Legendre quadrature, proposed by Biegler-König et al., is used for the integration of the coordinates.[33,38]

It is always said that the bisection search succeed by mediation of the mean value theorem. However, it must be noted that the bisection method defined above is coupled to a flux integration for the bracketing process. It is at this step that the above method finds difficulties in some topologies. More specifically, and as advanced above, the integration of core shells entails serious problems due to the planarity of the ELF profile around the shells (see inset for the direction perpendicular to the NaBr interionic axis in Figure 1). The nearly nonzero derivative distorts the Newton−Raphson flux integration, that in the best of these cases provides an inaccurate attractor position, complicating the coordinates comparison for the bisecant point discarding, or even worse integrates to a wrong point. The punctual core attractors of the crystal (shells > K) descend from a perturbation induced by the environment of the atomic shells in vacuo, where they are organized in a degenerated sphere. The potential from the nearby attractors gives rise to a collapse onto the (3, −3) shell attractors. This is due to the changes in the density and the kinetic energy upon the long-range influence of an external potential. These increments are magnified along the interattractor direction (r), where the term $\partial\phi/\partial r$ is vanishingly small, being ϕ the interacting molecular orbital.[45] This steepest increase in the density and decrease in the kinetic energy in the parallel direction gives rise to an increase in the ELF and, therefore, to the attractor collapse on the internuclear line. In general, the greater the potential, the larger the deformation and the easier the integration of the shell basin. As depicted in the inset for method II in Figure 1, the deviation of the (3, −3) points is greater than that of the connecting (3, −1) points. This is easily taken into account by the perturbative changes explained above, whose effect is shifting the attractor towards the source of the potential.

If more shells are present in the core, the intermediate ones are subject to the attractive potential from the neighboring nuclei as well as the repulsive potential from other shell attractors, and more complicated topological patterns may arise (e.g. ligand opposed core charge concentrations).[46,47] However, in these cases, the distances are large enough as to induce very little deformations and the spherical shape is nearly preserved. Hence, once again, the most complicated computational situations arise from inner core shells of heavy atoms as well as from ionic interactions. A change of gradient search procedure is not convenient due to the fact that the integration only fails along a certain angular interval. Therefore, a complementary integration method seems more appropriate. At this point, a previous proposal of the authors[48] to take the basin shells of solids as one chemically meaningful superbasin holds the key for the design of the integration procedure. From a conceptual point of view, the partition of core into basins is a mere consequence of symmetry. Furthermore, it has been shown that this split is not chemically meaningful[48] but just a mere artifact induced by the symmetry. If all the basins belonging to the same shell are integrated together, the approximated sphericity, for which the above bisection was developed, is recovered, and so are the curved ELF profiles. This algorithm is designated as method II in Figure 1 and is most appropriate for the integration of densities in outer shells, such as the M- and L-shell of Br^- on the figure. Besides, this method increases the accuracy of the integrations, other-

Table 1. Set of Critical Points Found for an Ionic (fcc LiF, $a = 4.017$ Å) and a Covalent Crystal (diamond C, $a = 3.102$ Å)[a]

LiF							C (diamond)						
Type	*x*	*y*	*z*	M	η	CHM	Type	*x*	*y*	*z*	M	η	CHM
(3, −3)	0.0000	0.0000	0.0000	4	0.9999	C(Li)	(3, −3)	0.1250	0.1250	0.1250	8	0.9999	C(C)
(3, −3)	0.5000	0.5000	0.5000	4	0.9999	C(F)	(3, −3)	0.0000	0.2500	0.2500	16	0.9352	V(C,C)
(3, −3)	0.0000	0.1256	0.5000	24	0.8555	V(F)	(3, −1)	0.0745	0.3750	0.3750	48	0.5954	C−V
(3, −1)	0.5000	0.2500	0.2500	24	0.0280	F−F	(3, −1)	0.0710	0.1790	0.1783	32	0.0833	V−V
(3, −1)	0.5000	0.4114	0.4114	48	0.8549	V(F)−V(F)	(3, +1)	0.2403	0.2403	0.2405	32	0.4675	ring
(3, −1)	0.1805	0.0000	0.0000	24	0.1463	Li−F	(3, +1)	0.0293	0.1250	0.1250	48	0.0736	ring
(3, −1)	0.4548	0.0000	0.0000	24	0.1303	C(F)−V(F)	(3, +1)	0.2500	0.2500	0.5000	16	0.0427	ring
(3, +1)	0.1804	0.3196	0.3196	32	0.1533	ring	(3, +3)	0.3750	0.3750	0.3750	8	0.0236	cage
(3, +1)	0.0000	0.3576	0.3576	48	0.0095	ring	(3, +3)	0.1829	0.1829	0.1779	32	0.0670	cage
(3, +1)	0.4277	0.5723	0.5723	32	0.8548	ring							
(3, +1)	0.4681	0.4681	0.4988	48	0.1303	ring							
(3, +3)	0.2500	0.2500	0.2500	8	0.0129	cage							
(3, +3)	0.1210	0.3790	0.3790	32	0.0083	cage							
(3, +3)	0.4739	0.0261	0.9739	32	0.1303	cage							
Morse				0							0		

[a] Positions (*x*, *y*, *z*), multiplicities (M), ELF value at the CP (η), and chemical meaning (CHM) are collected.

Table 2. Set of Critical Points Found for a Metallic (fcc Al, $a = 4.086$ Å) and a Molecular Crystal ($Pa\bar{3}$ N_2, $a = 5.0$ Å)[a]

Al							N_2						
type	*x*	*y*	*z*	M	η	CHM	type	*x*	*y*	*z*	M	η	CHM
(3, −3)	0.0000	0.0000	0.0000	4	0.9999	K(Al)	(3, −3)	0.0530	0.0530	0.0530	8	0.9999	C(N)
(3, −3)	0.5000	0.5000	0.2738	24	0.6805	V(Al)	(3, −3)	0.0226	0.4774	0.4553	24	0.8867	V(N, N)
(3, −3)	0.3035	0.3035	0.0000	48	0.7234	V(Al)	(3, −3)	0.6402	0.3598	0.8629	8	0.9868	V(N)
(3, −3)	0.0000	0.4246	0.5000	24	0.8697	L(Al)	(3, −3)	0.4626	0.0374	0.5000	24	0.8842	V(N, N)
(3, −1)	0.2500	0.5000	0.2500	24	0.3011	V−V	(3, −1)	0.4022	0.9025	0.4401	24	0.7187	V(N)−V(N, N)
(3, −1)	0.4440	0.0000	0.4495	96	0.8697	L-L	(3, −1)	0.2155	0.5415	0.2721	24	0.0050	N_2−N_2
(3, −1)	0.3402	0.3402	0.1520	96	0.6379	V−V	(3, −1)	0.9734	0.5266	0.4734	8	0.1227	C−V
(3, −1)	0.4467	0.4467	0.0000	48	0.8696	L−L	(3, −1)	0.4200	0.9200	0.5801	8	0.1334	C−V
(3, −1)	0.0000	0.0000	0.9723	24	0.1891	C−V	(3, +1)	0.3507	0.3507	0.3507	8	0.0003	ring
(3, +1)	0.3281	0.3281	0.3232	32	0.0691	ring	(3, +1)	0.1740	0.3713	0.2015	24	0.0007	ring
(3, +1)	0.4100	0.4100	0.8838	96	0.0486	ring	(3, +1)	0.0081	0.4925	0.3435	24	0.6382	ring
(3, +1)	0.5000	0.0258	0.4900	96	0.1891	ring	(3, +1)	0.0000	0.5000	0.5000	4	0.8664	ring
(3, +3)	0.2500	0.2500	0.2500	8	0.0391	cage	(3, +1)	0.5301	0.4700	0.9075	24	0.0543	ring
(3, +3)	0.1729	0.5000	0.5000	24	0.0470	cage	(3, +3)	0.2890	0.2890	0.2890	8	0.0002	cage
(3, +3)	0.5000	0.5000	0.5000	4	0.0004	cage	(3, +3)	0.5000	0.5000	0.5000	4	0.0001	cage
							(3, +3)	0.9275	0.5727	0.4900	24	0.0540	cage
							(3, +3)	0.4901	0.9230	0.5669	24	0.0532	cage
							(3, +3)	0.0771	0.0099	0.0667	24	0.0532	cage
Morse sum				0							0		

[a] Positions (*x*, *y*, *z*), multiplicities (M), ELF value at the CP (η), and chemical meaning (CHM) are collected.

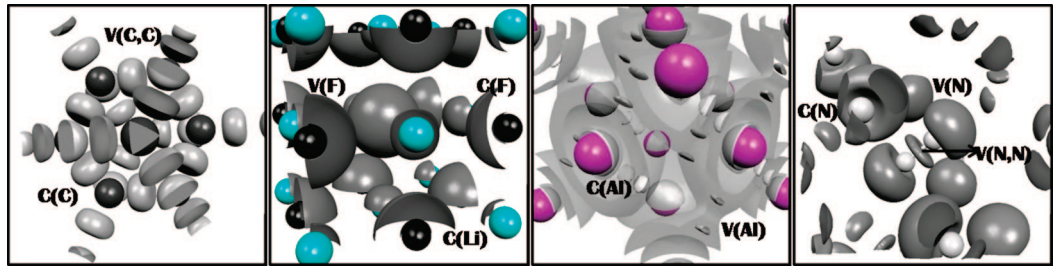

Figure 3. Schematic ELF profile of the various type of solids (see text): (a) diamond, (b) LiF, (c) Al, (d) N_2.

wise endangered by the low performance of the quadrature at high density cusp points,[40] and fastens the general procedure, since less integrals in low symmetry crystals are needed. For this purpose, the assignation of basin attractors to a certain nucleus turns out to be crucial, allowing the bipartition procedure to be applicable in spite of the basin attractor and the center of integration not being the same.

As the number of shells increases, the potential induced by the environment is screened and the inner shells remain degenerated. Hence, the above bipartition procedures are no longer applicable, since it fails to accurately locate the extremes. Furthermore, the bracketing of the bisection becomes extremely complicated due to the clustering of inner separatrices. The combination of the above algorithms is to be complemented by a third method in the case of heavy

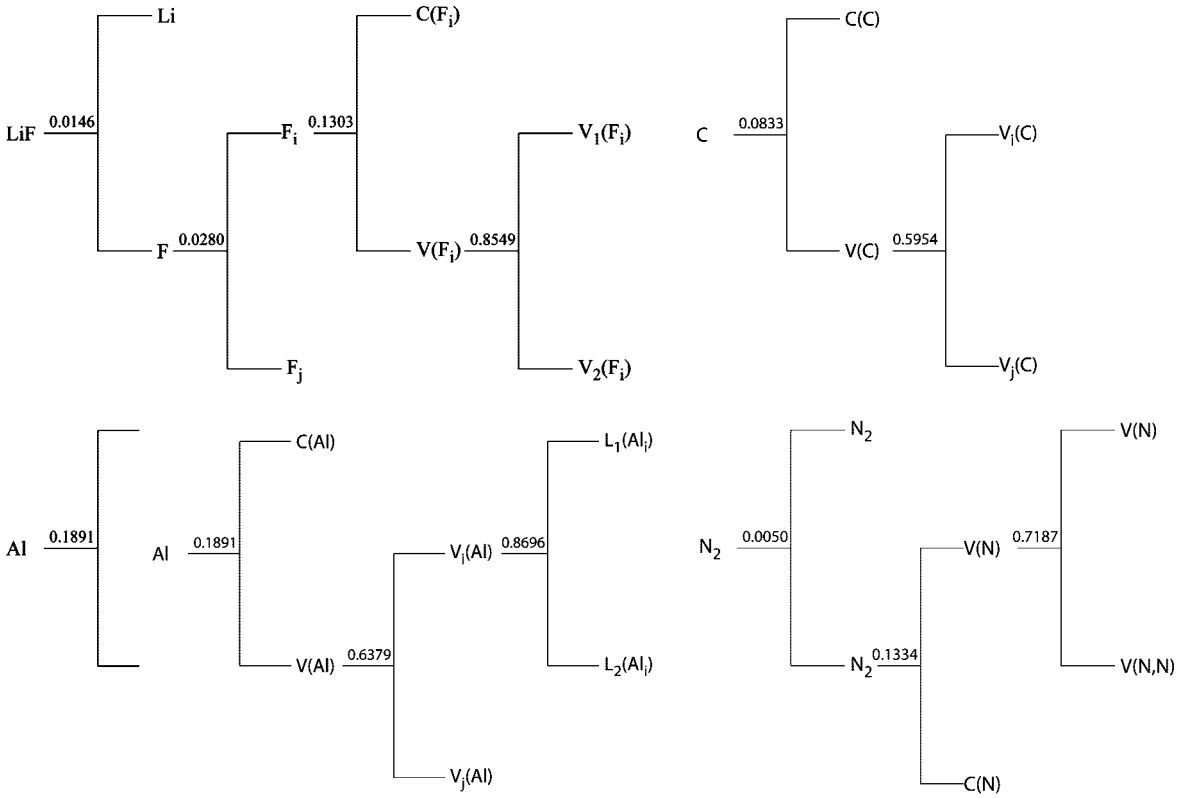

Figure 4. Bifurcation tree for LiF, C, Al, and N_2. The crystal data is as in Tables 1 and 2, respectively.

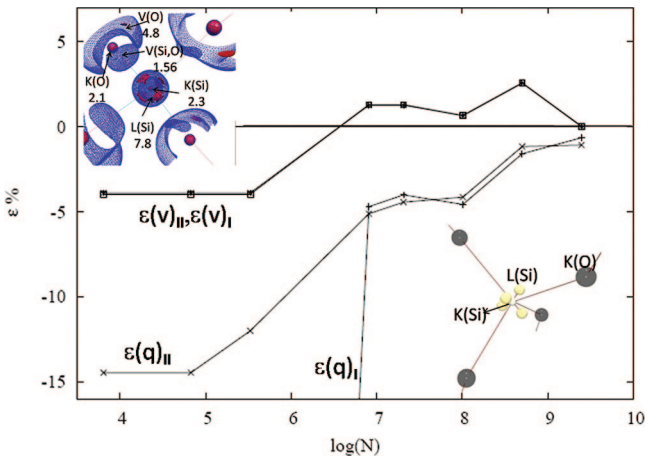

Figure 5. Convergence of ELF basin charges in the cristobalite phase of SiO_2 for an $n = n_r \times n_\theta \times n_\phi$ grid. The meaning of the basin labels is illustrated in the upper left inset: K stands for the 1st shell, L, for the 2nd, V(Si, O), for bond, and V(O), for lone pair. Curves present the relative error, ϵ (%), in the integration of charges (ϵ_q) and volumes (ϵ_v) according to both methods of integration (labeled I and II). Inset in the right bottom corner is an illustration of the complementary tetrahedral distribution of oxygens (black) and L-shell maxima (yellow online).

elements (from the 3rd and 4th rows downward). Taking into account that the problems in these shells arise from their spherical shape, the approximation (method III) of $\partial\eta/\partial\vec{r}$ by $\partial\eta/\partial r$ becomes a reasonable approach to the correct answer, as depicted in Figure 1 for the 1st K-shell of Br^-.

All the program features and main operation routines are schematized in Figure 2. First, the autocritic routine localizes the critical points of the cell by means of the combined core−valence algorithm. The characterization of the topology induced by the ELF gradient is used for studying the interactions in the solid. Then, the basin integration implemented in integrals is coupled to the CP search (represented by the arrow shape in the diagram) and makes use of all three algorithms described above to provide charge and volume values associated to the maxima found in the first step. Finally, the construction of η and $\nabla\eta$ grids with the doplot routine enables the bonding pattern of the solid to be visually analyzed.

IV. Performance

A. Critical Points. Lists of critical points for compounds representative of ionic, covalent, metallic, and molecular bonding are gathered in Tables 1 and 2. Multiplicities, referred to in the tables as "M", have to be taken into account to check the Morse sum. The corresponding ELF pictures and bifurcation trees are displayed in Figures 3 and 4. As explained above, these trees have a dual purpose in the analysis of the bonding: on the one hand, they highlight chemical units, and on the other hand, they unveil the nature of the interaction between them.

LiF in Table 1a is characterized by the absence of bond basins, only showing core and valence closed-shell basins (C(Li), C(F), and V(F)) whose shape approach that of a sphere (see Figure 3), as can be shown from the small variance in the critical point distance to the nucleus. It should be noted that, contrary to some early ideas, clear quantifiable ELF topological difference arises for the polarity of ionic compounds. Among these compounds, polarity can be viewed as an especial orientation of the valence toward the

Table 3. Calculated Charges (q_i) and Volumes (V_i) of ELF Basins in LiF (fcc, $a = 4.017$ Å) C (diamond, $a = 3.56$ Å), Al (fcc, $a = 4.086$ Å), and N_2 ($Pa\bar{3}$, $a = 5.0$ Å) for an $n_r \times n_\theta \times n_\phi$ grid of $30 \times 15 \times 15$[a]

	LiF		C		Al		N_2	
basin	q_i	V_i	q_i	V_i	q_i	V_i	q_i	V_i
core(A)	2.03	14.02	2.08	0.79	10.01	9.89	2.08	0.45
core(B)	2.15	0.17						
bond			1.98	20.39			3.50	26.48
lone pair							3.18	159.34
valence	7.81	98.57			2.99	111.64		
ε	−0.1%	−1.3%	+0.08%	−2.3%	−0.4%	0.3%	+0.2%	0.9%

[a] Errors (ϵ) in percent are with respect to the total volume and number of electrons per formula unit. A and B stand for Li and F, respectively.

atoms with whom it is bonded. The difference between the ELF values at the maxima and intrashell bip points gives an idea of the delocalization between the basins of the valence:[48] $\Delta\eta^{\mathrm{val}} = \eta^{\mathrm{val}}_{(3,-3)} - \eta^{\mathrm{val}}_{(3,-1)_{\mathrm{intra}}}$. Further information on the calculation of ionic polarity can be found by another article of the authors,[48] where this index is applied in order to track the subtle variation of ionicity along the B1 → B3 of BeO. In Figure 4, the hierarchy of the basins for LiF is built from these results. It can be seen that the first reduction corresponds to cation−anion separation at a very low ELF value (represented in the tables as Li−F) so that the crystal has no common valence. The stabilization of the compound comes therefore from electrostatic grounds. The high value at which the F valence domains are split clearly shows that they form one meaningful chemical unit, that is, the L-shell.

A covalent solid like diamond (Table 1 and Figure 3) displays a continuous 3D-network of tetrahedrically coordinated carbons, C(C), bound together by means of single-bond basins, V(C, C). The first domain separation (Figure 4) gives rise to cores and a common valence, formed by the bonds, at ELF = 0.08 (C(C)−V(C, C)). The valence domain is separated into irreductible bond basins at 0.59 (V(C, C)−V(C, C)). It can be seen from Figure 3 that metallic Al is formed of two shells (C(Al) and V(Al)). The quantitative results in Table 2a show that the valence of the atom is spread over the crystal, giving rise to low ELF maxima. Furthermore, the valence bips also show a value close to 0.5, so that the resulting bifurcation tree reveals a nearly continuous and planar valence (Figure 4) The observation of this planarity in the valence ELF in many metals led Silvi and Gatti to establish the characterization of metallic bond in terms of the delocalization window: $^6\Delta\eta\mathrm{val} = \eta^{\mathrm{val}}_{(3,-3)} - \eta^{\mathrm{val}}_{(3,-1)}$, yielding 0.043 for the Al. As far as N_2 is concerned, the value of ELF at the intermolecular points (named "N_2−N_2" in Table 2) is crucial in order to study the relationship between the molecular units. As reflected in Figure 4, the van der Waals forces that stabilize the crystal give rise to a first reduction into N_2 molecular units at this very low intermolecular ELF value, whereas the covalency within molecules is revealed by the common valence they share (formed by bonds, V(N, N), and lone pairs V(N)).

Overall, the relevance of the (3, −1) points and the necessity of a reliable code for the localization of all the valence critical points, cannot be overemphasized. Furthermore, the identification and characterization of the complete set of critical points are of capital importance in the study of chemical change by means of the catastrophe theory, a field that up to now, and due to the lack of a computational method, was restricted to the molecular realm.[49,50]

B. Basin Integration. The cristobalite phase of silica has been chosen to exemplify the performance of the integrations. It constitutes one of the simplest examples whereby all kinds of ELF basins can be found.[47] Cristobalite SiO_2 presents three maxima of ELF near the oxygen centers. One corresponds to the lone pair basin with 4.8 electrons. The other two are bonding basins sharing an average of 1.56 electrons with each of the silicon centers to which O is coordinated (see upper left inset in Figure 5). Silicon inner cores (with 2.3 electrons) are surrounded by the L-shell split in 4 maxima, giving a total charge for the outer core of 7.8 electrons. These maxima are located against the positions of the oxygens[47] (see bottom right inset in Figure 5), corresponding to a feature of the laplacian called ligand opposed core charge concentrations (LOCCC).[46] Hence, they reflect in an indirect and subtle way the 4-fold coordination of Si in cristobalite.

The integration grid for each basin consisted from 5 to 40 points for the radial and angular integrations, respectively. The logarithm of the total number of grid points is represented on the x axis of Figure 5. A convergence to the tenths of electrons and hundredths of volume atomic units, which is enough for most common applications, is usually found by a mixture of methods I and II (and III if heavy elements are present) with a $n_r \times n_\theta \times n_\phi$ grid of $30 \times 15 \times 15$ points. In spite of the modest amount of points, this grid provides volumes that fill up the volume of the cristobalite unit cell with errors around 0.8%. Greater deviations are encountered in the charge due to core integrations, where the high density value at the quadrature points gives rise to bigger inaccuracies. Indeed, the convergence obtained in the volume integration of SiO_2 with both methods is nearly the same, but it decreases when charge density is integrated from 1.1% to 0.7% if both methods are combined (see Figure 5). Deviations are also expected in specially challenging cases where the low symmetry of the cell or the split of multiple bonds demand greater grids. The number of gradient evaluations is of the order of 10^5 for each nonequivalent basin or group of basins, so any additional simplification of the integration turns out to be extremely valuable. In this sense, method number II for outer core integrations not only gives rise to greater accuracy but also provides great time saving by integrating all atomic shells together and requiring smaller grids. Another way to fasten the calculations is the use of cell symmetry: the

integration of basins occupying high symmetry Wyckoff positions can be limited to the irreducible angular part.

In order to check the applicability of integrations to different bonding patterns, the representative examples presented in the previous section have been considered following the hybrid procedure and using the selected 30 × 15 × 15 grid. Results are compiled in Table 3. It can be seen that the quantitative picture recovered by ELF in the solid state is in agreement with chemical expectations. The ionic nature of LiF is observed in its closed shell basins with a charge transfer of 0.97 electrons. The Ne-like core with 10 electrons in aluminum is perfectly recovered, as well as the metallic valence surrounding it, formed by unsaturated basins of small charge. The high pressure molecular phase of N_2 keeps a strong N−N bond with a charge of 3.5 electrons and voluminous lone pairs that fill the space and hold 3.18 electrons each. Lower population than that of a formal triple bond is expected due to the pressure induced charge flow from the bond basin to the lone pair and to the presence of resonant structures.[37] In the case of diamond, perfect electron pairs are found, according to the perfect covalency of the compound and the absence of resonant forms. The last row of Table 3 reveals that the percent error in the integrations stays below 0.5% in the charge and 2.5% in the volume, confirming the ability of the new algorithm to provide accurate charges and volumes for ELF basins in a wide range of solids. We firmly believe that the hereby proposed method will enable to extend the quantitative topological ELF analysis of bonding to the solid state, where the appearance of complex bonding structures claims for such approaches.

V. Conclusions

An algorithm for the complete characterization of the topology induced by ELF in solids, including identification and characterization of all critical points and basin integration, is put forward. It is based on the fact that this topology is characterized for having two regions with different topological features: on the one hand, the valence, which can be determined following previous crystalline topological methods, and on the other hand, the core, whose sphericity holds the key for designing new automated algorithms. The robustness of the approach is proved across a wide range of applications, where the relevancy of a thorough determination of the local and global properties of the electron localization function is well set. The next step toward a deeper understanding of bond in solids and its dynamical change involves the calculation of probabilities[51] and localization/delocalization indexes,[29,52] dependent on higher order density matrices.

Acknowledgment. Financial support from the Spanish MEC and FEDER programs under projects MAT2006-13548-C02-02 and CTQ-2006-02976 and Programa Ingenio 2010 under the MALTA-Consolider CSD2007-00045 project are gratefully acknowledged. J.C.-G. thanks the Spanish MEC for a FPU postgraduate grant.

References

(1) Mori-Sánchez, P.; Martín Pendás, A.; Luaña, V. *J. Am. Chem. Soc.* **2002**, *124*, 14721.

(2) Savin, A.; Jepsen, O.; Flad, J.; Andersen, O. K.; Preuss, H.; von Schnering, H. G. *Angew. Chem., Int. Ed. Engl.* **1992**, *31*, 187.

(3) Bader, R. F. W. *Atoms in Molecules: A Quantum Theory*; Oxford Univ. Press: Oxford, 1990.

(4) Martín Pendás, A.; Costales, A.; Luaña, V. *Phys. Rev. B* **1997**, *55*, 4275.

(5) Gatti, C. *Zeit. Kristallogr.* **2005**, *220*, 399.

(6) Silvi, B.; Gatti, C. *J. Phys. Chem. A* **2000**, *104*, 947.

(7) Savin, A. *J. Phys. Chem. Solids* **2004**, *65*, 2025.

(8) Gibbs, G. V.; Cox, D. F.; Boisen, M. B., Jr.; Downs, R. T.; Ross, N. L. *Phys. Chem. Minerals* **2003**, *30*, 305.

(9) Gibbs, G. V.; Cox, D. F.; Ross, N. L. *Phys. Chem. Minerals* **2004**, *31*, 232.

(10) Nathaniel, O.; Malcom, J.; Popelier, P. L. A. *J. Comput. Chem.* **2003**, *24*, 437.

(11) Becke, A. D.; Edgecombe, K. E. *J. Chem. Phys.* **1990**, *92*, 5397.

(12) von Weizsäcker, C. F. *Z. Phys.* **1935**, *96*, 431.

(13) Savin, A.; Becke, A. D.; Flad, J.; Nesper, R.; Preuss, H.; von Schnering, H. G. *Angew. Chem., Int. Ed. Engl.* **1991**, *30*, 409.

(14) Savin, A.; Nesper, R.; Wengert, S.; Fässler, T. F. *Angew. Chem., Int. Ed. Engl.* **1997**, *36*, 1809.

(15) Burdett, J. K.; McCormick, T. A. *J. Phys. Chem. A* **1998**, *102*, 6366.

(16) Nalewajski, R. F.; Koster, A. M.; Escalante, S. *J. Phys. Chem. A* **2005**, *109*, 10038.

(17) Dobson, J. F. *J. Chem. Phys.* **1991**, *94*, 4328.

(18) Kohout, M.; Pernal, K.; Wagner, F. R.; Grin, Y. *Theor. Chem. Acc.* **2004**, *112*, 453.

(19) Kohout, M.; Pernal, K.; Wagner, F. R.; Grin, Y. *Theor. Chem. Acc.* **2005**, *113*, 287.

(20) Silvi, B. *J. Phys. Chem. A* **2003**, *107*, 3081.

(21) Matito, E.; Silvi, B.; Duran, M.; Solà, M. *J. Chem. Phys.* **2006**, *125*, 024301.

(22) Silvi, B. *Phys. Chem. Chem. Phys.* **2004**, *6*, 256.

(23) Lewis, G. N. *Valence and the Structure of Atoms and Molecules*; Dover: New York, 1966.

(24) Abraham, R. H.; Marsden, J. E. *Foundations of Mechanics*; Addison Wesley: Reading, MA, 1994.

(25) Silvi, B.; Savin, A. *Nature* **1994**, *371*, 683.

(26) Häussermann, U.; Wengert, S.; Nesper, R. *Angew. Chem., Int. Ed. Engl.* **1994**, *33*, 2069.

(27) Martín Pendás, A.; Francisco, E.; Blanco, M. A. *Chem. Phys. Lett.* **2008**, *454*, 396.

(28) Calatayud, M.; Andrés, J.; Beltrán, A.; Silvi, B. *Theor. Chem. Acc.* **2001**, *105*, 299.

(29) Savin, A.; Silvi, B.; Colonna, F. *Can. J. Chem.* **1996**, *74*, 1088.

(30) Kohout, M.; Savin, A. *Int. J. Quantum Chem.* **1996**, *60*, 875.

(31) Mezey, P. G. *Can. J. Chem.* **1993**, *72*, 928.

(32) Kohout, M.; Wagner, F. R.; Grin, Y. *Theor. Chem. Acc.* **2002**, *108*, 150.

(33) Biegler-Köonig, F. W.; Bader, R. F. W.; Tang, T.-H. *J. Comput. Chem.* **1982**, *3*, 317.

(34) Otero de la Roza; A.; Blanco, M. A.; Martín Pendás; A.; Luaña, V. *Comput. Phys. Commun.* **2009**, *180*, 157.

(35) Silvi, B. *J. Mol. Struct.* **2002**, *614*, 3.

(36) Contreras-García, J.; Martín Pendás, A.; Silvi, B.; Recio, J. M. *J. Phys. Chem. Solids* **2008**, *69*, 2204.

(37) Contreras-García, J.; Silvi, B.; Martín Pendás, A.; Recio, J. M. *J. Phys. Chem. B*, in press.

(38) Biegler-König, F. W.; Nguyen-Dang, T. T.; Tal, Y.; Bader, R. F. W. *J. Phys. B: Atom. Molec. Phys.* **1981**, *14*, 2739.

(39) Popelier, P. L. A. *Mol. Phys.* **1996**, *87*, 1169.

(40) Popelier, P. L. A. *Comput. Phys. Commun.* **1998**, *108*, 180.

(41) Rafat, M.; Popelier, P. L. A. *J. Comput. Chem.* **2007**, *28*, 2602.

(42) Noury, S.; Krokidis, X.; Fuster, F.; Silvi, B. *Comput. Chem.* **1999**, *23*, 597.

(43) Nathaniel, O.; Malcom, J.; Popelier, P. L. A. *J. Comput. Chem.* **2003**, 24.

(44) Henkelman, G.; Arnaldsson, A.; Jonsson, H. *Comput. Mater. Sci.* **2006**, *36*, 354.

(45) Feinberg, M. J.; Ruedenberg, K. *J. Chem. Phys.* **1971**, *54*, 1495.

(46) Bytheway, I.; Gillespie, R. J.; Tang, T.-H.; Bader, R. F. W. *Inorg. Chem.* **1995**, *34*, 2407.

(47) Gracia, L.; Contreras-García, J.; Beltrán, A.; Recio, J. M. *High Pres. Res.*, in press.

(48) Contreras-García, J.; Silvi, B.; Martín Pendás, A.; Recio, J. M. *J. Phys. Chem. B* **2008**, *112*, 9787.

(49) Krokidis, X.; Noury, S.; Silvi, B. *J. Phys. Chem. A* **1997**, *101*, 7277.

(50) Polo, V.; Andres, J.; Castillo, R.; Berski, S.; Silvi, B. *Chem.—Eur. J.* **2004**, *10*, 5165.

(51) Savin, A. *J. Chem. Sci.* **2005**, *117*, 473.

(52) Chesnut, D. B. *Chem. Phys.* **2001**, *271*, 9.

CT800420N